Results in Materials 20 (2023) 100469

Contents lists available at ScienceDirect

Results in Materials

journal homepage: www.sciencedirect.com/journal/results-in-materials

Analysis of K_4ZnAs_2 Zintl phased ternary semiconductor compound for optoelectronic application

Samuel Wafula , Robinson Musembi *, Francis Nyongesa

Monolith Research Group, Department of Physics, Faculty of Science and Technology, University of Nairobi, P.O. Box 30197, 00100, Nairobi, Kenya

ARTICLE INFO

Keywords:
DFT
K_4ZnAs_2
Ternary compounds
Zintil phase
Optoelectronics
Pnictide
Photovoltaic

ABSTRACT

In this study, Zintl phased tetrapotassium diarsenidozincate K_4ZnAs_2 semiconductor compound was analysed using ab initio methods for structural, electronic, mechanical, elastic, and optical properties using six exchange correlation functionals: LDA-PZ, GGA-BLYP, GGA-EV, GGA-PBE, GGA-PBESol, and SO-GGA. The bandgap of the material was found to range from 0.5493 eV to 1.2282 eV, with the predicted bandgap lying within the visible region, suggesting that the material is suitable for optoelectronic applications in photovoltaics. The electronic structure analysis of the projected density of states showed that the valence band formation was mainly dominated by As 2*p*, Zn 2*p*, Zn 1*s*, and K 2*s*, with other orbitals making minor contributions, whereas the conduction band formation was mainly formed by Zn 1*s* and Zn 2*p*, with low contributions from As 2*p* and K 2*s* orbitals, with the other orbitals making insignificant contributions. The material was ductile, mechanically stable, ionic, and anisotropic when subjected to external forces. The optical properties showed that the material exhibited excellent absorption within the visible region, which supports the results obtained for the bandgap. The average lattice parameter was $a = 18.2477$, which is in good agreement with the experimental results reported in the literature.

1. Introduction

The optoelectronic industries currently compete to produce devices with good energy conversion efficiency and low power consumption because these are the factors attracting most consumers [1–3]. This desire has not gone unnoticed within the scientific community, where there has been an increase in scientific research for obtaining exemplary semiconductor materials with desirable qualities such as high power conversion efficiency, high temperature stability, tuneable band gap, high dielectric constant, and perfect performance for applications in an advanced range of technological fields such as optoelectronics, thermoelectric, spintronics, photodetectors, biomedical imaging, and etc [4,5]. Semiconductor markets mostly comprise inorganic materials such as silicon, gallium arsenide, cadmium telluride, organic, and organic/inorganic fused structures [6]. However, inorganic compounds dominate the market because of their high photon-electron conversion efficiency and stability [6]. The numerous properties of these materials have been studied. Nevertheless, the purity of production, optoelectronic potential, intrinsic stability, eco-friendliness, and conversion efficiency of such materials remain under-researched [7]. This provides room for extensive study to obtain new classes of materials, such as ternary chalcogenides [8], ternary pnictides [9], and hybrid anion-cation fused compounds [10], to provide generalised insight into the properties of numerous semiconductor compounds.

In the recent years, Zintl clusters have attracted great and ongoing interest because of the properties they possess, they have rich diversity of structures, unique reactivity, intriguing chemical bonding, and application in material science [11–13]. The structural diversity emanates from large variety in permutation and combinations between the classical A-B binary Zintl phased compounds (where A = electropositive alkali, alkaline or rare earth metal, B = electronegative main group elements), the combination has been greatly extended to ternary Zintl ABX structure by introducing X as transition metal elements [12]. The resulting ABX ternary compounds commonly rationalised using the Wade-Mingos rules and Zintl-Klemm concepts. There are wide range of metal fluxes (example Sn, Sb, Zn, In, Ga, Al, and Bi), where the phase diagrams for Na–Sb, K–As, K–Sb, and K–Bi binary systems show that ternary compounds can easily be synthesised [11,14].

Compounds similar to the one under study have been reported in the literature, where they have been synthesised and their crystal structures have been analysed experimentally, such as K_4CdAs_2 [15], K_4HgAs_2 [16], and K_4BeP_2 [17] In a different study, Eisenmann and Somer

* Corresponding author.
E-mail address: musembirj@uonbi.ac.ke (R. Musembi).

https://doi.org/10.1016/j.rinma.2023.100469
Received 1 September 2023; Received in revised form 26 September 2023; Accepted 1 October 2023
Available online 7 October 2023

studied the structural and vibrational analysis of intermetallic compounds of Na_4HgP_2, K_4ZnP_2, K_4CdP_2 and K_4HgP_2, these materials are reported to be isosteric anions of $HgCl_2$ compound [18]. In an earlier literature report by Prots et al. [19], an experimental work was reported for synthesis and analysis of K_4ZnAs_2 Zintl phased ternary compound. Despite the existence of the experimental work, a theoretical analysis detailing the properties of this material has not been done before and therefore this informed our motivation to study the material by first principles method. In this study, in order to carefully study the material and predict reliable parameters ab initio calculations were performed using six exchange-correlation functionals, namely the LDA-PZ, GGA-PBE, GGA-PBEsol, GGA-BLYP, GGA-EV, and GGA-SO. This study brings to the fore important insight into the scientific world by making useful data available so that the next level of application can be undoubtfully be tackled.

2. Computational techniques

The calculations in this work were performed using the plane-wave self-consistence field method, PWscf, using the density functional theory method, as implemented in the quantum espresso computational code which uses first-principles techniques [20,21]. The generalised gradient approximation method and the local density approximation method were used as the exchange-correlation potential [22], with two types of exchange-correlation functionals adopted for the work: ultra-soft-core correction with scalar relativistic type or the norm-conserving scalar relativistic type. The functional used for the local density approximation computation was the Perdew-Zunger LDA-PZ [23], while those based on the generalised gradient approximation used were GGA-BLYP (Becke-Lee-Yang-Parr) [24], GGA-EV (Engel-Vosko) [25], GGA-PBE (Perdew-Burke-Ernzerhof) [26], GGA-PBESol (Perdew-Burke-Ernzerhof for solids) [27], and SO-GGA (second-order GGA) [28]. The procedure for obtaining the crystallographic information file and processing the input files has been described previously [29]. The lattice parameters, kinetic energy cut-off, and Monkhorst-Pack [30] k-point mesh were optimised, including the variable cell relaxation, before the actual computation was performed. The optimised kinetic energy cut-off with respect to the total energy was set at 140 Ry, whereas the final Monkhorst-Pack k-point mesh used in this work was optimised at $9 \times 9 \times 9$ with an offset of 0. Additionally, geometry optimisation was performed by minimising the total energy with respect to the lattice parameter and then fitting the data to the Birch-Murnaghan equation of state, as reported elsewhere [31]. The optimum parameters were then used to calculate the electronic band structure, density of states (including the projected density of states), and mechanical and optical properties of the compound material.

3. Results and discussion

3.1. Structural properties

The tetrapotassium diarsenidozincate K_4ZnAs_2 semiconductor compound has a trigonal crystal structure belonging to R-3m space group number 166, this material crystallises into rhombohedral lattice with lattice parameters $a = b = 5.75$ Å, $c = 26.78$ Å which agrees very well with experimental work reported by Prots et al. (2007) [19]. The mean lattice parameter from the six functionals was $a = 18.2477$ a. u., which is in good agreement with the experimental value of 18.2170 a. u. reported in the literature for the synthesised K_4ZnAs_2 compound [19]. The structure of this material has two inequivalent K^{1+} sites, with the first K^{1+} site attached to three equivalent As^{3-} atoms in a trigonal, non-coplanar geometry. In the first case, all K–As bond lengths are 3.47 Å. At the second K^{1+} site, K^{1+} is bound to four equivalent As^{3-} atoms to form a mixture of edge- and corner-sharing $K–As^4$ tetrahedra. There is one shorter (3.34 Å) and three longer (3.50 Å) K–As bond lengths. Zn^{2+} is bound to two equivalent As^{3-} atoms in a linear geometry. Both Zn–As bond lengths are 2.33 Å. As^{3-} is bound to seven K^{1+} and one Zn^{2+} atom in a distorted cubic centering geometry [32].

Table 1
Computed ground-state lattice parameters, bulk modulus, equilibrium volumes, and enthalpies of formation of K_4ZnAs_2 ternary compound using various correlation functionals.

	Lattice parameter a_o (a.u)	Bulk modulus B_o GPa	Equilibrium volume (a.u)^3	Enthalpy of formation ΔH_f (Ry)
LDA	17.5986	7.2	5450.47	−419.77
PBE	18.2247	5.3	6053.12	−424.58
PBESol	17.9182	6.0	5752.81	−416.69
BLYP	18.5201	4.7	6352.32	−423.90
EV	19.8910	3.2	7869.87	−429.09
SOGGA	17.3333	8.5	5207.72	−439.79
Other work	18.2170			

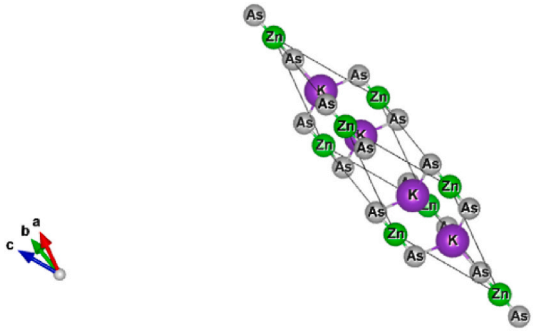

Fig. 1. Crystal structure of Zintl phased K_4ZnAs_2 ternary compound.

The crystal structure parameters including: the lattice a parameter, bulk modulus, equilibrium volume, enthalpy of formation energy were calculated by fitting the lattice parameter vs total energy, and cell volume vs total energy using the Birch-Murnaghan equation of state given by equation (1).

$$E(V) = E_o + \frac{B}{B'(B'-1)}\left[V\left(\frac{V_o}{V}\right)^{B'} - V_o\right] + \frac{B}{B'}(V - V_o) \quad (1)$$

where in equation (1), E_o, B, B′, V, and V_o are respectively, the optimum value of total energy, the bulk modulus, the pressure derivative of bulk modulus, the total unit cell volume, and the optimised unit cell volume. The results are given in Table 1.

3.2. Electronic properties

The optimum parameters obtained from the variable cell relaxation and lattice parameter optimisation were used to calculate the electronic properties of the trigonal phase of K_4ZnAs_2 (see Fig. 1). To understand the electronic properties of the compound, ground state conditions were used to calculate the density of states, and the band structures of the trigonal phase of the K_4ZnAs_2 structure were investigated along the symmetry points (Γ, T, $H_2|H_0$, L, F $S_0|S_2$, F, Γ) in the Brillouin zone using GGA-PBE, GGA-PBEsol, PZ-LDA, GGA-BLYP, GGA-EV, and GGA-SO as exchange-correlation functionals. At the Fermi level E_F (E = 0), the material was noted to have an indirect band gap where the minima of the valence band were at the gamma point, while the maxima of the conduction band were at the F-symmetry point for all functionals used, confirming that K_4ZnAs_2 is a semiconductor material. The electronic band structure indicates the band gap type of the material which is a crucial parameter that determines the type of application and suitability in optoelectronics. The obtained density of states and band diagrams for the K_4ZnAs_2 trigonal structure for the GGA-PBE, GGA-PBEsol, PZ-LDA,

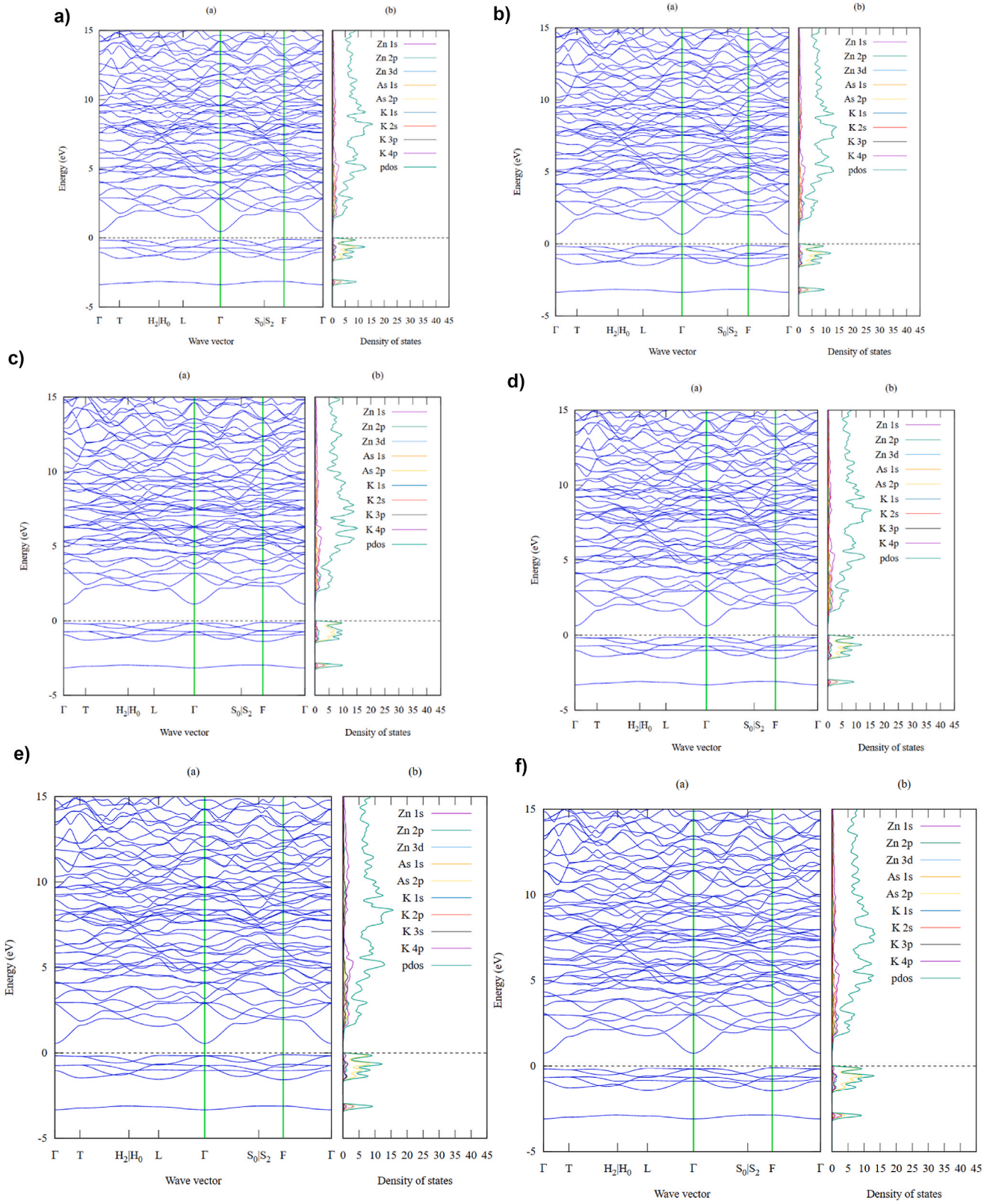

Fig. 2. aLDA-PZ calculated band diagram and projected density of states for K4ZnAs2 compound with Eg = 0.5493 eV
b: GGA-BLYP calculated band diagram and projected density of states for K4ZnAs2 compound with Eg = 0.7724 eV
c: GGA-EV calculated band diagram and projected density of states for K4ZnAs2 compound with Eg = 1.2282 eV
d: GGA-PBE calculated band diagram and projected density of states for K4ZnAs2 compound with Eg = 0.7215 eV
e: GGA-PBESol calculated band diagram and projected density of states for K4ZnAs2 compound with Eg = 0.6565 eV
f: SO-GGA calculated band diagram and projected density of states for K_4ZnAs_2 compound with Eg = 0.8526 eV.

Table 2
Elastic tensor in GPa for K_4ZnAs_2 orthorhombic crystal structure.

	C_{11}	C_{12}	C_{13}	C_{14}	C_{33}	C_{44}	C_{66}
LDA	25.58	7.58	4.30	0.78	36.7	4.54	9.00
PBE	27.50	9.50	5.98	0.78	37.4	4.44	8.98
PBESol	27.47	9.19	6.11	0.75	38.6	4.68	9.14
BLYP	26.54	8.83	6.00	0.76	37.2	4.52	8.86
EV	36.03	16.0	12.8	0.82	45.6	4.36	10.0
SOGGA	41.3	20.2	12.7	0.43	47.3	5.25	10.5

GGA-BLYP, GGA-EV, and GGA-SO functionals are shown in Fig. 2a–f.

The smallest bandgap ($E_g = 0.5493$ eV) was obtained using LDA-PZ, which is known to underestimate the bandgap of materials, while the largest bandgap ($E_g = 1.2282$ eV) was obtained using GGA-EV which has an advantage in predicting a good bandgap for semiconductor materials [33]. The other functional predicted bandgaps of 0.7724 eV (GGA--BLYP), 0.7215 eV (GGA-PBE), 0.6565 eV (GGA-PBESol), and 0.8526 eV (SO-GGA). This study provides good insight into the bandgap of the material because of the use of a variety of functionals, each having its own intrinsic strength which sets it apart from the others. This material structure also exhibited no discontinuities throughout the chosen k-paths, as observed in Fig. 2 a-f. By calculating the density of states (DOS) of this material, we can determine the available electronic states/shell/orbitals that an electron can occupy for a given atom to contribute to band-edge formation. The six functionals used in the analysis of the electronic properties of K_4ZnAs_2 were as follows: the valence band was mainly formed by the Zn-2*p*, Zn-3*d*, As-1*s* and As-2*p* orbitals, with very small contributions from the other orbitals. The upper conduction band is mainly formed by K-4*p*, K-3*p*, K-1*s*, Zn-3*d*, Zn-2*p*, and Zn-1*s* orbitals, with little contribution from the other states. The dispersion characteristics of the conduction and valence bands indicated a strong interaction between the orbitals of the seven atoms of the K_4ZnAs_2 structure. The interaction of the orbitals results in the hybridisation of different states, leading to the formation of a bandgap within the structure. These interactions are essential for optoelectronic and photovoltaic applications, because they prevent optical transitions with the same electronic states to take place. This allows for maximum optical absorption in the visible region of the light energy spectrum.

3.3. Elastic and mechanical properties

The elastic properties are important for determining the structural, thermal, and mechanical stability of materials. Moreover, the elastic properties also provide information on how a material responds to both the intrinsic and extrinsic forces applied to its crystal structure. Mechanical stability was obtained by confirming the elastic constants C_{ij}. Other elastic properties, such as bulk modulus B, shear modulus G, Young's modulus E, and Poisson's ratio *n*, were also computed in this study. The elastic constants of the trigonal K_4ZnAs_2 structure were computed by using GGA-PBE. GGA-PBEsol, PZ-LDA, GGA-BLYP, GGA-EVE, and GGA-SO functionals. The K_4ZnAs_2 ternary material adopts rhombohedral (I) crystal structure belonging to Laue class $\bar{3}m$ featuring 6 independent elastic constants given as C_{11}, C_{12}, C_{13}, C_{22}, C_{33}, C_{44}, and C_{66}. The most important and fundamental conditions for the elastic stability of rhombohedral lattice systems are given by Equation (2), while the elastic tensor values are given in Table 2. The calculations show that trigonal K_4ZnAs_2 satisfies the necessary and sufficient conditions; therefore, the material is mechanically stable, and the mechanical properties are obtained from the Voigt-Reuss-Hill average approximation criterion [34].

$$\begin{cases} C_{11} > |C_{12}|, C_{44} > 0 \\ C_{13}^2 < \frac{1}{2}C_{33}(C_{11} + C_{12}) \\ C_{14}^2 < \frac{1}{2}C_{44}(C_{11} - C_{12}) \equiv C_{44}C_{66} \end{cases} \quad (2)$$

Table 3
Voigt-Reuss-Hill average mechanical properties, bulk modulus B, Young's modulus E, Shear modulus G, Pugh's ratio B/G, Poisson's ratio *n*, and Debye temperature θ_D.

	B	E	G	B/G	*n*	θ_D K
LDA	13.30	19.07	7.58	1.76	0.26	172.8
PBE	14.97	19.20	7.47	2.00	0.28	173.4
PBESol	15.06	19.75	7.72	1.95	0.27	175.3
BLYP	14.56	19.06	7.44	1.96	0.28	174.1
EV	22.2	20.9	7.81	2.84	0.34	179.6
SOGGA	24.4	23.7	8.87	2.75	0.34	189.4

The Voigt-Reuss-Hill average mechanical properties for bulk modulus B and shear modulus G in the rhombohedral phase were calculated using the elastic stiffness tensor C_{ij} and elastic compliance tensor S_{ij} as given by equations (3) and (4) respectively, the calculated values for the K_4ZnAs_2 are as given in Table 3.

$$B = \frac{B_V + B_R}{2} = \frac{1}{2}\left[\frac{1}{9}(2C_{11} + 2C_{12} + 4C_{13} + C_{33}) + \frac{1}{(2S_{11} + 2S_{12} + 4S_{13} + S_{33})}\right] \quad (3)$$

$$G = \frac{G_V + G_R}{2} = \frac{1}{2}\left[\frac{1}{30}(7C_{11} - 5C_{12} - 4C_{13} + 2C_{33} + 12C_{44}) + \frac{1}{(2S_{11} + 2S_{12} + 4S_{13} + S_{33})}\right] \quad (4)$$

The parameters used to define the mechanical properties, as shown in Table 3, were consistently higher for the EV-GGA and SO-GGA functionals. The bulk modulus measures the resistance to the change in volume that occurs because of the external pressure applied to the material. The larger the value of the bulk modulus, the harder is the material. Based on the calculated bulk moduli using the six functionals, we predict that the K_4ZnAs_2 material is a soft material because, in all cases, the value of the bulk modulus is not very large.

The ductility and brittleness of a material were determined using Pugh's [35] and Poisson's ratio [36]. A material is said to be brittle if the B/G ratio is less than 1.75, whereas if the material has a B/G ratio greater than 1.75, it implies that the material is ductile. The results obtained using these six functionals confirmed that the material was ductile. Furthermore, the covalent or ionic properties of the material can be predicted using the Poisson's ratio n, for covalent material, the condition $0 < n < 0.25$ is true, and ionic if $0.25 < n < 0.5$ is true. Because the Poisson's ratios of the six functionals used were approximately greater than 0.25 and less than 0.5, this implies that K_4ZnAs_2 has ionic properties. These findings are in agreement with data in the literature [37–39]. The bulk modulus is a measure of the resistance to volume changes due to the application of external pressure. The shear modulus measures the incompressibility, whereas the Young's modulus measures the stiffness of a material. Large values of B, G, and E imply that the material is stiff and incompressible, and the data presented in Table 3 show that K_4ZnAs_2 is less stiff and does not present a strong resistance to compression force. This analysis shows that the properties of K_4ZnAs_2 are suitable for application in areas where it will face expansion and contraction without easy cracking, as in the case of photovoltaics which are exposed to harsh conditions.

Directional isotropy or anisotropy refers to the directional dependency of the mechanical properties which is closely analogous to the plastic deformation and crack characteristics of a material. In this study, to obtain a comprehensive insight into the elastic isotropy/anisotropy of the K_4ZnAs_2 compound, the spatial dependencies of the Young's modulus, shear modulus, and Poisson's ratio were calculated, as shown in graphical representation in Fig. 3 a-c.

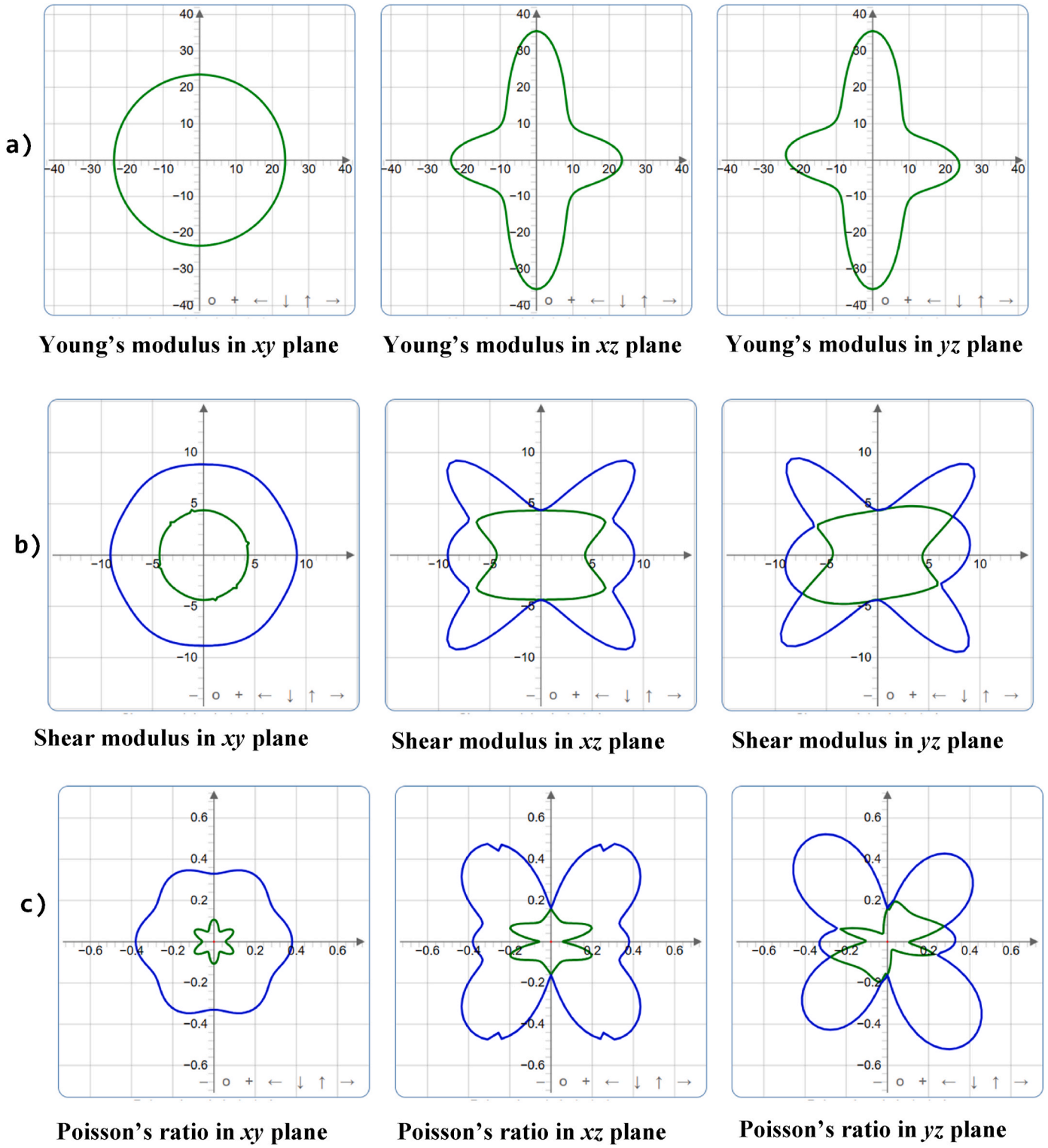

Fig. 3. The spatial dependency of (a) Youngs modulus, (b) Shear modulus, and (c) Poisson's ratio The degree of anisotropy is dependent on the deviation of a geometrical body from the spherical shape in this case, represented in a 2D shape. If a geometrical body is a spherical (3D) or circular (2D) shape, it exhibits isotropy, which is observed in the *xy*-plane for Young's modulus, shear modulus, and Poisson's ratio at varying degrees. It is also observed that for the *xz*-plane, the degree of anisotropy is more symmetric for Young's modulus, shear modulus, and Poisson's ratio, whereas for *the yz*-plane, the anisotropy displays an antisymmetric distribution. The anisotropic variation for the calculated values of Young's modulus were 12.749 GPa and 35.502 GPa for the minimum and maximum values, respectively, while the shear modulus and Poisson's ratio were 4.31 GPa,12.63 GPa and 0.045, 0.627 for the minimum and maximum values. This variation represents anisotropy values of 2.785, 2.929, and 13.8346 for the Young's modulus, shear modulus, and Poisson's ratio, respectively. The low values obtained here corroborate the earlier deduction that the material is ductile [40]. In summary, the K_4ZnAs_2 compound displays isotropy in the *xy*-plane but anisotropy in the *xz* and *yz* planes.

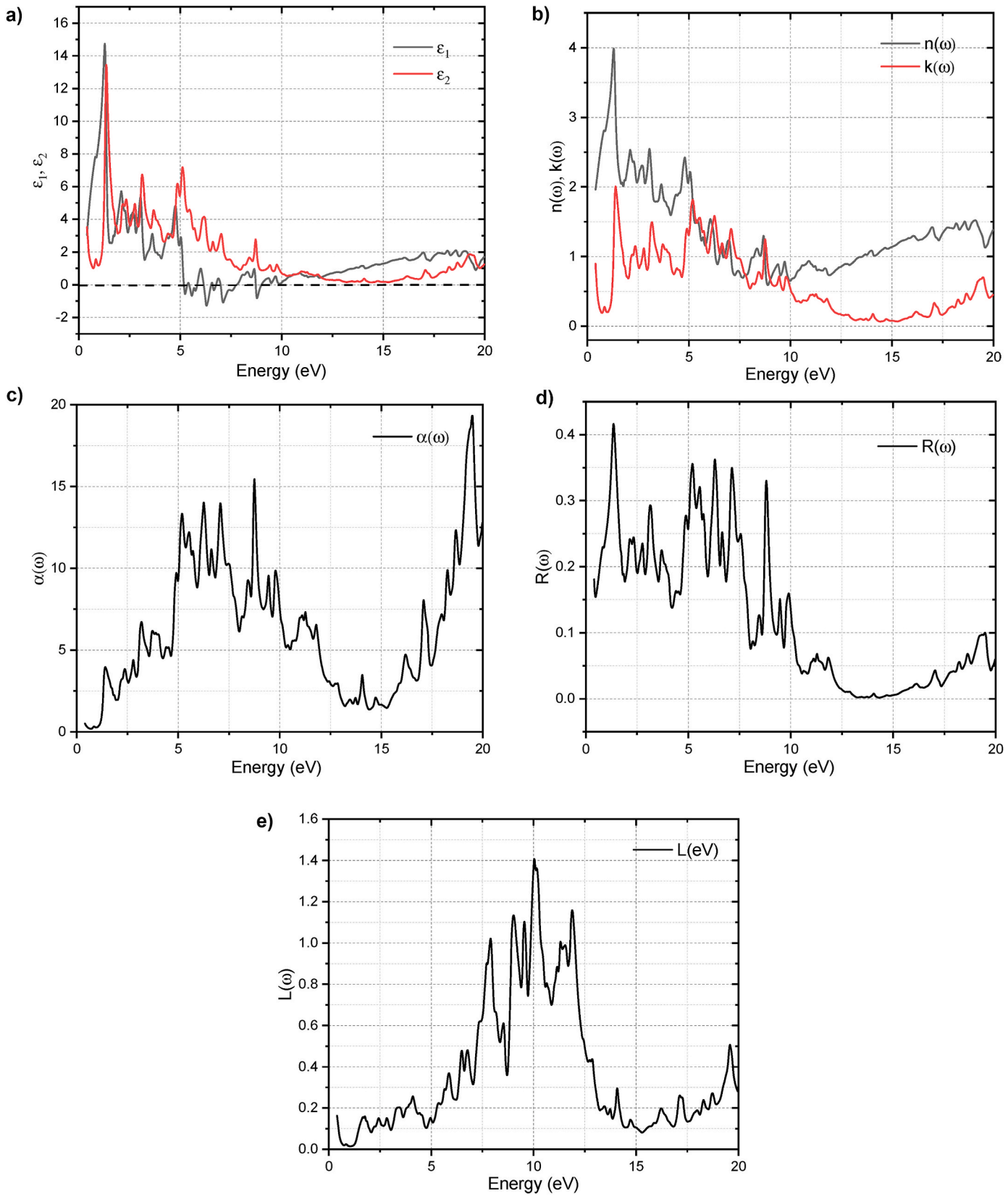

Fig. 4. a: Dielectric constants as a function of energy for K4ZnAs2
b: Refractive index and extinction coefficient as a function of energy for K4ZnAs2
c: Absorption coefficient as a function of energy for K4ZnAs2
d: Reflectivity as a function of energy for K4ZnAs2
e: Energy loss function as a function of energy for K_4ZnAs_2.

3.4. Optical properties

The optical properties of semiconductors are important because they determine how they interact with electromagnetic spectral radiation. This is the basis for technologies such as optical communication, displays, and optical storage. The optical properties depend on the band structure of semiconductors, which affects the optical permittivity and absorption coefficient, and their analysis can further extend our understanding of their suitability for optoelectronic and photovoltaic applications. In this study, crucial parameters were analysed to understand the suitability of this material. The results obtained for the optical properties are shown in Fig. 4(a–e).

The complex dielectric wave equation explains the response of the electrons of the material to the incident photon energy and is given by Equation (5).

$$\varepsilon(\omega) = \varepsilon_1(\omega) + \varepsilon_2(\omega) \tag{5}$$

where $\varepsilon(\omega)$ is the total angular frequency dependent dielectric function, $\varepsilon_1(\omega) = n^2 - k^2$ is the real part of the complex dielectric wavefunction with n and k being the refractive index and extinction coefficient respectively, and $\varepsilon_2(\omega) = 2nk$ is the imaginary part of the dielectric function. The $\varepsilon_1(\omega)$ defines the wave damping and energy dissipation, whereas the imaginary part $\varepsilon_2(\omega)$ is related to polarization and is responsible for the phonon absorption in a material.

The dielectric functions for this material showed that it was higher at lower energy from 1.0 eV to 7.0 eV and beyond there it dramatically decreases, indicating that the materials exhibit strong attenuation of the incident electromagnetic wave radiation within this region, and therefore exhibit metallic characteristics. The refractive index n(ω) and extinction coefficient k(ω) are important optical parameters for studying the potential applications of materials in optical and photonic devices [41]. The expressions for the refractive index and extinction coefficients are given by Equations (6) and (7), respectively.

$$n(\omega) = \frac{1}{2}\left(\varepsilon_1(\omega) + \left(\varepsilon_1^2(\omega) + \varepsilon_2^2(\omega)^{1/2}\right)\right)^{1/2} \tag{6}$$

$$k(\omega) = \frac{1}{2}\left(-\varepsilon_1(\omega) + \left(\varepsilon_1^2(\omega) + \varepsilon_2^2(\omega)^{1/2}\right)\right)^{1/2} \tag{7}$$

Refractive index n (ω) is a useful parameter for predicting light refraction, particularly in optoelectronic applications. When photons come into contact with matter, they slow down owing to their interaction with electrons, and their refractive index is greater than one. However, if photons pass through a material with a higher refractive index n(ω), more photons are attenuated. There is a tendency for n (ω) to increase when the electronic density is increased. The extinction coefficient k(ω) is analogous to ε_2(ω), as observed in Fig. 4a and b, and the dissimilarity of k(ω) from ε_2(ω) is ascribed to the slight differences in optical conductivity [42]. In photonics, the extinction coefficient k(ω) is an important attribute of the fluorescence phenomenon; when the extinction coefficient is large, the fluorescence is proportionately high.

The other optical parameters used in this study are the absorption coefficient, reflectivity, and energy loss function, as given in equations (8)–(10), and used in Fig. 4c, d, and 4e, respectively. The absorption coefficient measures the amount of light energy absorbed by a material. Reflectivity describes the surface characteristics of a material, while the energy-loss spectrum highlights the energy loss of electrons entering the material.

$$\alpha(\omega) = \sqrt{2}(\omega)\left(\sqrt{\varepsilon_1^2(\omega) + \varepsilon_2^2} - \varepsilon_1(\omega)\right)^{1/2} \tag{8}$$

$$R(\omega) = \left(\frac{[n(\omega) - 1]^2 + k(\omega)^2}{[n(\omega) + 1]^2 + k(\omega)^2}\right) \tag{9}$$

$$L(\omega) = \frac{\varepsilon_2(\omega)}{\varepsilon_1^2(\omega) + \varepsilon_2^2(\omega)} \tag{10}$$

The absorption coefficient is an important parameter which is closely related to the skin depth of the material in which the electromagnetic waves interact with. Fig. 4c shows a graphical representation of the calculated absorption coefficient of the K_4ZnAs_2 compound which spans from the deep ultraviolet region at 20 eV to the infrared region. The wide absorption range of this material is an important characteristic desirable for applications in the optoelectronic and photovoltaic industries. The absorption spectra $\alpha(\omega)$ can be used to explain the case of absorption of the incident photon energy. It measures the quantity of light energy absorbed by the material. The computed spectra of $\alpha(\omega)$ for K_4ZnAs_2 are presented in Fig. 4c. In the spectra of $\alpha(\omega)$, it is shown that initially the value of $\alpha(\omega)$ is zero, and the peaks start appearing from around 0.71eV which corroborates earlier values obtained for the electronic bandgap. The absorption spectrum of K_4ZnAs_2 had a wide range of 1.5–14.5 eV spanning the UV–Vis range and again at 16 eV–20 eV.

The optical surface properties of a material are best described using reflectivity characteristics. In Fig. 4d, the reflectivity of the K_4ZnAs_2 compound is highest between 0 eV and 11 eV, which corroborates the observation of the absorption coefficient in Fig. 4c as well as the energy loss function, as shown in Fig. 4e.

Major energy loss peaks were observed in the slightly higher energy region of approximately 7–13 eV. No energy loss peaks were observed in the visible region. No significant peaks were observed in the visible region.

4. Conclusion

The structural, electronic, mechanical, elastic, and optical properties of trigonal K_4ZnAs_2 ternary pnictide structures were studied using the first-principles method with triangulation of six exchange correlation functionals: LDA-PZ, GGA-PBE, GGA-PBESol, GGA-EV, GGA-BLYP, and SO-GGA. The material has been predicted to be thermodynamically and mechanically stable, with bandgaps ranging between 0.5493 and 1.2282 eV. The lattice parameter and bandgap values were in agreement with previous experimental and theoretical studies, respectively. The conduction band formation was found to be mainly due to Zn 1*s* and Zn 2*p*, with low contributions from the As 2*p* and K 2*s* orbitals, and the other orbitals making insignificant contributions. On the other hand, the valence band formation is mainly due to the As 2*p* orbital, with some significant contributions from Zn 2*p*, Zn 1*s*, and K 2*s*, and other orbitals making minor contributions. The results revealed that K_4ZnAs_2 absorbs light energy within the UV-VIS region of the electromagnetic spectrum as well as in the infrared region, showing excellent potential for optoelectronic and photovoltaic applications.

CRediT authorship contribution statement

Samuel Wafula: Conceptualization, Data curation, Formal analysis, Investigation, Methodology, Writing – original draft, and writing. **Robinson Musembi:** Conceptualization, Data curation, Formal analysis, Investigation, Methodology, writing, Validation, Visualization, Supervision, Software, review and editing, review and editing. **Francis Nyongesa:** Conceptualization, Data curation, Formal analysis, Investigation, Methodology, writing, Validation, Visualization, Supervision.

Declaration of competing interest

The authors declare that they have no known competing financial interests or personal relationships that could have appeared to influence the work reported in this paper.

Data availability

Data will be made available on request.

Acknowledgements

The authors acknowledge the RSIF grant number RSIF_RA_005 and RSIF_RA_015 for support in some of the resources used in this work, International Science Program for computational seed grant through KEN02 grant, the Centre for High Performance Computing CHPC, RSA for computing resources.

References

[1] C. Zhu, et al., "Optical synaptic devices with ultra-low power consumption for neuromorphic computing,", Light Sci. Appl. 11 (1) (2022) 337, https://doi.org/10.1038/s41377-022-01031-z.
[2] Jun Li, J. Buckwalter, Energy efficiency of optoelectronic interfaces in scaled FinFET and SOI CMOS technologies, in: 2015 IEEE Optical Interconnects Conference (OI), IEEE, 2015, pp. 18–19, https://doi.org/10.1109/OIC.2015.7115666.
[3] P. Xu, Z. Zhou, "Silicon-based optoelectronics for general-purpose matrix computation: a review,", Advanced Photonics 4 (4) (2022) https://doi.org/10.1117/1.AP.4.4.044001.
[4] A. Chaves, et al., "Bandgap engineering of two-dimensional semiconductor materials,", NPJ 2D Mater Appl 4 (1) (2020) 29, https://doi.org/10.1038/s41699-020-00162-4.
[5] N. Ali, et al., "Advances in nanostructured thin film materials for solar cell applications,", Renew. Sustain. Energy Rev. 59 (2016) 726–737, https://doi.org/10.1016/j.rser.2015.12.268.
[6] L. El Chaar, L.A. lamont, N. El Zein, "Review of photovoltaic technologies,", Renew. Sustain. Energy Rev. 15 (5) (2011) 2165–2175, https://doi.org/10.1016/j.rser.2011.01.004.
[7] Q. Zhang, W. Hu, H. Sirringhaus, K. Müllen, Recent progress in emerging organic semiconductors, Adv. Mater. 34 (22) (2022), 2108701, https://doi.org/10.1002/adma.202108701.
[8] R. Kormath Madam Raghupathy, H. Wiebeler, T.D. Kühne, C. Felser, H. Mirhosseini, Database screening of ternary chalcogenides for P-type transparent conductors, Chem. Mater. 30 (19) (2018) 6794–6800, https://doi.org/10.1021/acs.chemmater.8b02719.
[9] J.M. Cameron, R.W. Hughes, Y. Zhao, D.H. Gregory, Ternary and higher pnictides; prospects for new materials and applications, Chem. Soc. Rev. 40 (7) (2011) 4099, https://doi.org/10.1039/c0cs00132e.
[10] Y.-L. Wei, J. Jing, C. Shi, H.-Y. Ye, Z.-X. Wang, Y. Zhang, High quantum yield and unusual photoluminescence behaviour in tetrahedral manganese(II) based on hybrid compounds, Inorg. Chem. Front. 5 (10) (2018) 2615–2619, https://doi.org/10.1039/C8QI00793D.
[11] O. Janka, S.M. Kauzlarich, "Zintl compounds,", in: Encyclopedia of Inorganic and Bioinorganic Chemistry, Wiley, 2021, pp. 1–19, https://doi.org/10.1002/9781119951438.eibc0244.pub3.
[12] F. Gascoin, S. Ottensmann, D. Stark, S.M. Haïle, G.J. Snyder, Zintl phases as thermoelectric materials: tuned transport properties of the compounds CaxYb1-xZn2Sb2, Adv. Funct. Mater. 15 (11) (2005) 1860–1864, https://doi.org/10.1002/adfm.200500043.
[13] J.D. Corbett, "Polyanionic clusters and networks of the early p-element metals in the solid state: beyond the Zintl boundary,", Angew. Chem. Int. Ed. 39 (4) (2000) 670–690, https://doi.org/10.1002/(SICI)1521-3773, 20000218.
[14] Q. Qin, L. Zhou, Y. Wang, R. Sang, L. Xu, Linear triatomic [ZnBi2]4− in K4ZnBi2, Dalton Trans. 43 (16) (2014) 5990, https://doi.org/10.1039/c3dt53419g.
[15] B. Eisenmann, J. Klein, M. Somer, Crystal structure of tetrapotassium diarsenidocadmate, K4CdAs2, Z. für Kristallogr. - Cryst. Mater. 197 (1–4) (1991) 271–272, https://doi.org/10.1524/zkri.1991.197.14.271.
[16] M. Asbrand, B. Eisenmann, M. Somer, Crystal structure of tetrapotassium diarsenidomercurate(II), K4[HgAs2], Z. Kristallogr. N. Cryst. Struct. 212 (1997), https://doi.org/10.1524/ncrs.1997.212.jg.79.
[17] M. Somer, M. Hartweg, K. Peters, H.G. von Schnering, Crystal structure of tetrapotassium diphosphidoberyllate, K4BeP2, Z. Kristallogr. 192 (3–4) (1990) 263–264, https://doi.org/10.1524/zkri.1990.192.3-4.263.
[18] B. Eisenmann, M. Somer, Intermetallische Verbindungen mit HgCl2 -isosteren Anionen: strukturelle und schwingungsspektroskopische Untersuchung von Na4HgP2, K4ZnP2 , K4CdP2 und K4HgP2, Z. Naturforsch. B Chem. Sci. 44 (10) (1989) 1228–1232, https://doi.org/10.1515/znb-1989-1015.
[19] Y. Prots, U. Aydemir, S.S. Öztürk, M. Somer, Crystal structure of tetrapotassium diarsenidozincate, K4ZnAs2, Z. Kristallogr. N. Cryst. Struct. 222 (3) (2007) 163–164, https://doi.org/10.1524/ncrs.2007.0067.
[20] P. Giannozzi, S. de Gironcoli, P. Pavone, S. Baroni, Ab initio calculation of phonon dispersions in semiconductors, Phys. Rev. B 43 (9) (1991) 7231–7242, https://doi.org/10.1103/PhysRevB.43.7231.
[21] P. Giannozzi, et al., Quantum espresso: a modular and open-source software project for quantum simulations of materials, J. Phys. Condens. Matter 21 (39) (2009), 395502, https://doi.org/10.1088/0953-8984/21/39/395502.
[22] P. Ziesche, S. Kurth, J.P. Perdew, Density functionals from LDA to GGA, Comput. Mater. Sci. 11 (2) (1998) 122–127, https://doi.org/10.1016/S0927-0256(97)00206-1.
[23] J.P. Perdew, A. Zunger, Self-interaction correction to density-functional approximations for many-electron systems, Phys. Rev. B 23 (10) (1981) 5048–5079, https://doi.org/10.1103/PhysRevB.23.5048.
[24] B. Miehlich, A. Savin, H. Stoll, H. Preuss, Results obtained with the correlation energy density functionals of becke and Lee, Yang and Parr, Chem. Phys. Lett. 157 (3) (1989) 200–206, https://doi.org/10.1016/0009-2614(89)87234-3.
[25] E. Engel, S.H. Vosko, Exact exchange-only potentials and the virial relation as microscopic criteria for generalized gradient approximations, Phys. Rev. B 47 (20) (1993) 13164–13174, https://doi.org/10.1103/PhysRevB.47.13164.
[26] J.P. Perdew, K. Burke, M. Ernzerhof, "Generalized Gradient Approximation Made Simple,", 1996.
[27] J.P. Perdew, et al., "Restoring the density-gradient expansion for exchange in solids and surfaces,", Phys. Rev. Lett. 100 (13) (2008), 136406 https://doi.org/10.1103/PhysRevLett.100.136406.
[28] Y. Zhao, D.G. Truhlar, Construction of a generalized gradient approximation by restoring the density-gradient expansion and enforcing a tight Lieb–Oxford bound, J. Chem. Phys. 128 (18) (2008), https://doi.org/10.1063/1.2912068.
[29] M. Mbilo, R. Musembi, First principles calculation to investigate the structural, electronic, elastic, mechanical, and optical properties of K2NiP ternary compound, AIP Adv. 12 (10) (2022), 105018, https://doi.org/10.1063/5.0118809.
[30] H.J. Monkhorst, J.D. Pack, Special points for Brillouin-zone integrations, Phys. Rev. B 13 (12) (1976) 5188–5192, https://doi.org/10.1103/PhysRevB.13.5188.
[31] M. Mbilo, R. Musembi, D.P. Rai, "First-principles study of properties of X3Sb2Au3 (X = K, Rb) ternary compounds for photovoltaic applications,", Indian J. Phys. 97 (8) (2023) 2355–2362, https://doi.org/10.1007/s12648-022-02547-1.
[32] A. Jain, et al., Commentary: the Materials Project: a materials genome approach to accelerating materials innovation, Apl. Mater. 1 (1) (2013), 011002, https://doi.org/10.1063/1.4812323.
[33] W. Khan, S. Goumri-Said, Engel-Vosko generalized gradient approximation within DFT investigations of optoelectronic and thermoelectric properties of copper thioantimonates(III) and thioarsenate(III) for solar-energy conversion, Phys. Status Solidi 253 (3) (2016) 583–590, https://doi.org/10.1002/pssb.201552435.
[34] F. Mouhat, F.-X. Coudert, Necessary and sufficient elastic stability conditions in various crystal systems, Phys. Rev. B 90 (22) (2014), 224104, https://doi.org/10.1103/PhysRevB.90.224104.
[35] S. Tariq, A. Ahmed, S. Saad, S. Tariq, Structural, electronic and elastic properties of the cubic CaTiO3 under pressure: a DFT study, AIP Adv. 5 (7) (2015), 077111, https://doi.org/10.1063/1.4926437.
[36] V. Kumar, B.P. Singh, "Structural and elastic properties of AIBIIIC 2 VI semiconductors,", Indian J. Phys. 92 (1) (2018) 29–35, https://doi.org/10.1007/s12648-017-1082-3.
[37] S. Ozdemir Kart, T. Cagın, "Elastic properties of Ni2MnGa from first-principles calculations,", J. Alloys Compd. 508 (1) (2010) 177–183, https://doi.org/10.1016/j.jallcom.2010.08.039.
[38] S. Sahin, Y.O. Ciftci, K. Colakoglu, N. Korozlu, "First principles studies of elastic, electronic and optical properties of chalcopyrite semiconductor ZnSnP2,", J. Alloys Compd. 529 (2012) 1–7, https://doi.org/10.1016/J.JALLCOM.2012.03.046.
[39] H. Bouafia, et al., Theoretical investigation of structural, elastic, electronic, and thermal properties of KCaF3, K0.5Na0.5CaF3 and NaCaF3 Perovskites, Superlattice. Microst. 82 (2015) 525–537, https://doi.org/10.1016/J.SPMI.2015.03.004.
[40] O. Gomis, F.J. Manjón, P. Rodríguez-Hernández, A. Muñoz, Elastic and thermodynamic properties of α-Bi2O3 at high pressures: study of mechanical and dynamical stability, J. Phys. Chem. Solid. 124 (2019) 111–120, https://doi.org/10.1016/j.jpcs.2018.09.002.
[41] M. Fox, G.F. Bertsch, Optical properties of solids, Am. J. Phys. 70 (12) (2002) 1269–1270, https://doi.org/10.1119/1.1691372.
[42] W. Khan, S. Azam, M.B. Kanoun, S. Goumri-Said, Optoelectronic structure and related transport properties of BiCuSeO-based oxychalcogenides: first principle calculations, Solid State Sci. 58 (2016) 86–93, https://doi.org/10.1016/j.solidstatesciences.2016.05.012.